Hollow Au/Ag Nanostars Displaying Broad Plasmonic Resonance and High Surface-Enhanced Raman Sensitivity

Adianez Garcia-Leis, [1] *Armida Torreggiani,* [2] *Jose Vicente Garcia-Ramos,* [1] *and Santiago Sanchez-Cortes*[1]*

[1] Instituto de Estructura de la Materia. IEM-CSIC, Serrano 121, 28006 Madrid, Spain.

[2] ISOF. Consiglio Nazionale delle Ricerche, Via P. Gobetti 101, 40129 Bologna, Italy.

*Corresponding author

Abstract

Bimetallic Au/Ag hollow nanostar (HNS) nanoparticles with different morphologies were prepared in this work. These nanoplatforms were obtained by changing the experimental conditions (concentration of silver and chemical reductors, hydroxylamine and citrate) and by using Ag nanostar as template nanoparticles (NPs) through galvanic replacement. The goal of this research was to create bimetallic Au/Ag star-shaped nanoparticles with advanced properties displaying a broader plasmonic resonance, a cleaner exposed surface, and a high concentration of electromagnetic hot spots on the surface provided by the special morphology of nanostars. The size, shape, and composition of Ag as well as their optical properties were studied by extinction spectroscopy, hyperspectral dark field microscopy, transmission and scanning electron microscopy (TEM and SEM), and energy dispersive X-ray spectroscopy (EDX). Finally, the surface-enhanced Raman scattering (SERS) activity of these HNS was investigated by using thioflavin T, a biomarker of the β-amyloid fibril formation, responsible for Alzheimer disease. Lucigenin, a molecules displaying different SERS activity on Au and Ag, was also used to explore the presence of these metals on the NPs surface. Thus, a relationship between morphology, plasmon resonance and SERS activity of these new NPs was made.

KEY WORDS: Hollow nanoparticles, nanostars, galvanic replacement, SERS, hyperspectral imaging, Thioflavin T.

INTRODUCTION

The fabrication of anisotropic metal nanoparticles (NPs) with large variety of sizes and shapes has been reported so far with promising applications in medicine, bio-imaging, and analyte detection.[1-11] In this regard, star-shaped NPs or metal nanostars (NS) have shown outstanding properties in the electromagnetic field intensification [12], that were recently applied in the design of SERS-based sensor devices based on localized surface plasmon resonance (LSPR).[10,13] These NPs represents a remarkable advance regarding spherical NP (SNP), since the existence of areas with large curvature where the electromagnetic field is highly enhanced,[14] makes unnecessary their aggregation, in contrast to what occurs for SNP.

Surprisingly, the main part of works published up to now about star-shaped nanosystems were accomplished by using NS made of Au (AuNS).[15] In addition, AuNS prepared so far generally require the use of surfactants and other compounds that remain partially adsorbed on the surface, thus limiting seriously their application in detection systems based on Surface-Enhanced Raman Scattering (SERS). Even so, these NS have been successfully applied in SERS but only in the detection of analytes able to give also a strong response on spherical NPs,[16-18] while the application in detection of challenging analytes is rather limited.

Recently, we have reported the fabrication silver nanostars (AgNS) with a high SERS activity[19]. The fabrication of NS made of silver has a large interest due to the interesting optical properties of this metal. These nanoparticles display high SERS performance because of two reasons: i) the easiness of analyte adsorption, since they exhibit clean adsorption surfaces, free from the strong surfactants usually employed to fabricate other types of nanostars,; and ii) the large intensification provided by their special morphology, thus making unnecessary the subsequent colloid aggregation.

Hollow nanoparticles (HNPs) have also attracted large attention in recent years. These NPs display very interesting plasmonic and catalytic proprieties, favorable for biomedical applications.[20-22] HNPs are usually obtained by galvanic replacement using Ag NPs as template.[23] In particular, Au nanocages were reported to be attractive theranostic platforms because they typically exhibit plasmons in the near-infrared (NIR) region. The latter is also called the "tissue therapeutic window" because of the lower optical attenuation from water and blood in this spectral range (650-900 nm), in comparison with that in the visible range[24]. However, hollow nanostars (HNS), an interesting system which could combine enhancing properties with theranostic advantages, were not fabricated up to know.

The present work was aimed at the fabrication of hollow bimetallic nanoparticles made of Au and Ag with the shape of stars, taking advantage of the two metals combination. Au/Ag hollow nanostars (Au/Ag HNS) were obtained by method combining the classical chemical reduction and the galvanic replacement method, using Ag nanostars as template prepared according to the method previously reported by us.[19] These bimetallic substrates have interesting optical properties because of the different plasmon activity of each metal. The plasmon resonance of Ag is localized in the blue region of the visible spectrum, while the Au resonance occurs in the red region. Therefore, the combination of both metals is advantageous to cover a broader LSPR region of the electromagnetic spectrum, thus enabling both sensing and theranostic applications of these new platforms.[25,26]

Different experimental conditions were probed for the fabrication protocol, in order to provide the formation of tailored nanostar-shaped substrates displaying a different optical response. The sensing ability of the resulting systems was monitored by using thioflavin T (ThT), a dye having a high selectivity for amyloid fibrils responsible

for the Alzheimer disease. In addition, Lucigenin, a viologen aromatic compound showing a different SERS spectrum on each metal (Au and Ag), was employed to investigate the metal composition of the surface of the resulting NPs.

EXPERIMENTAL METHODS

Chemicals: Silver nitrate ($AgNO_3$) was purchased from Merck. Hydroxylamine solution (50 w/w in water), sodium hydroxide, gold(III) chloride trihydrate ($HAuCl_4$), trisodium citrate (Na_3CIT), and Thioflavin T (ThT) were purchased from Sigma. Lucigenin (N,N'-Dimethyl-9,9'-biacridinium dinitrate) was purchased from Aldrich. All reagents used were of analytical grade. Milli-Q water (resistivity of 18 Ω) was used to dissolve all reagents and to obtain diluted solutions.

Preparation of hollow Au/Ag nanoparticles: Hollow Au/Ag NPs were prepared from starting Ag NPs in two steps that implies the previous formation of template Ag NS in a similar process as that reported by us.[19] In the first step of the process the neutral hydroxylamine (HA) was used as reducing agent, leading to the formation of faceted NPs (Fig. 1a). Five minutes after, an aqueous solution of $HAuCl_4$ was added (Fig. 1d), followed by a solution of citrate (CIT). The previous NPs acted as seeds for the formation of Ag NS obtained in the second step by CIT at high temperature (Fig. 1b). The reduction of Ag^+ with HA is not complete and a pool of unreduced Ag^+ ions still remains in solution, the remaining silver ions are then reduced by the addition of CIT leading to the formation of Ag NS as described in our previous work (…). After several attempts we have seen that the best result regarding morphology to obtain HNS is the simultaneous addition of $HAuCl_4$ and CIT. Ag NS are then converted into Au/Ag HNS (Fig. 1c) in the presence of Au^{3+} ions, which induce the Ag oxidation to Ag^+ in the Ag NS template by galvanic replacement because the standard reduction potential of $AuCl_4^-$/Au pair (0.99 V, vs SHE) is higher than that of

Ag^+/Ag pair (0.80 V, vs SHE)[27], thus leading to the formation of the resulting Au shell structure (Fig. 1e) according to the following process:

$$3\ Ag\ (s) + AuCl_4^-\ (aq) \longrightarrow Au(s) + 3\ Ag^+\ (aq) + 4\ Cl^-(aq) \qquad (1)$$

Afterwards, Ag^+ ions resulting from the galvanic replacement are again reduced to Ag^0 by citrate ions inducing the re-deposition of Ag atoms on the Au shell (Fig. 1f). Finally, the Au/Ag bimetallic shells are formed with the formation of an Au/Ag alloy with a thickness which depends on the experimental procedure (Fig. 1g). After the simultaneous addition of Au and CIT two different processes seems should occur: The growing of the initial NPs into Ag NPs and the galvanic replacement. The final nanostar shape of the resulting NPs indicates that the formation of Ag NS occurs first (Fig. 1a to b) and then the formation of the shell is taking place as shown in (Fig. 1b to c). The driving force for the formation of nanostar templates is the combined use of HA and CIT in a two-step preocess. The first step leads to the formation of faceted NPs from which CIT can induce the reduction and deposition of Ag on the faces of the initial NPs.

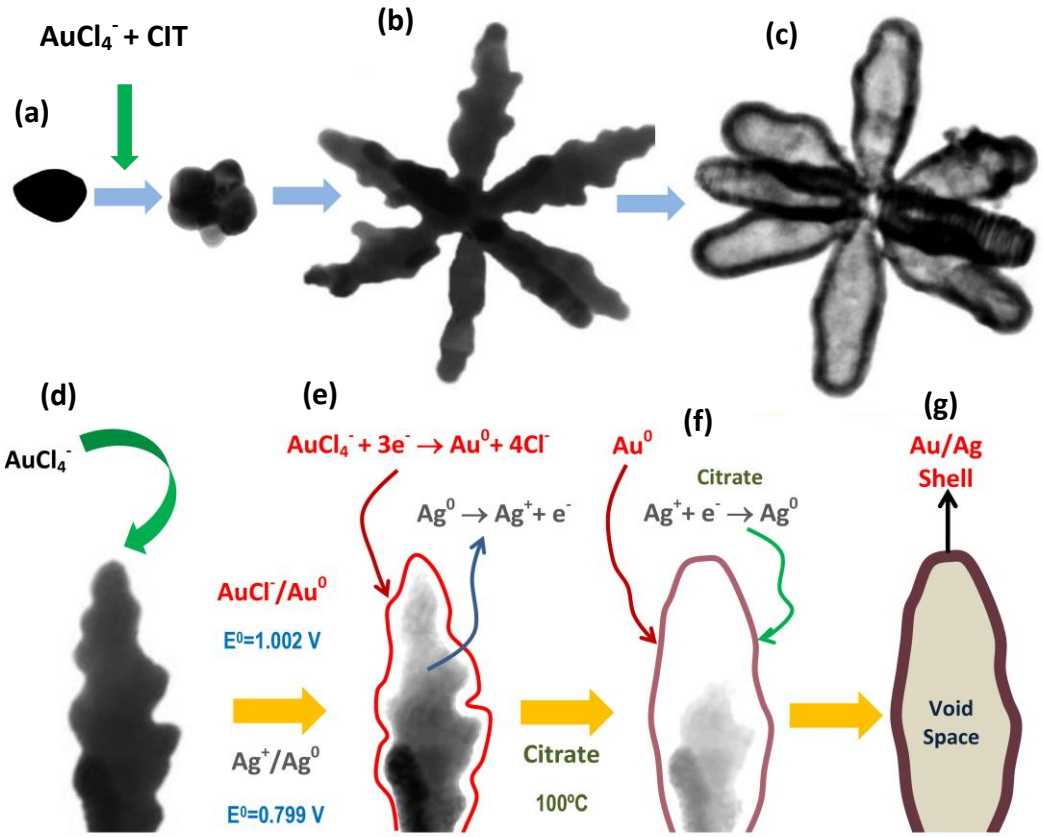

Figure 1. Up: (a-c) Schematic procedure suggested for the fabrication of Au/Ag hollow nanostars from Ag NS templates; Bottom: (d-g) Reaction mechanisms

suggested to explain the conversion of one AgNS arm into a hollow structure, by galvanic replacement and Ag redeposition induced by residual citrate.

Four preparation methods of bimetallic HNS were carried out in this work, giving rise to samples A-C and F. These methods involved the use of different relative concentrations of Ag^{+}, $AuCl_4^{-}$, HA, and CIT, as indicated in Table 1. In addition, nanoparticles of Au (Au NP) of samples D and E were used in control experiments. The sample D was prepared by successive reduction with HA and CIT as indicated below. The sample E was obtained with reduction with citrate according to the Fren's method.[28] Finally, Ag spherical nanoparticles (Ag NP), also employed as control, were prepared by reduction with hydroxylamine hydrochloride according to the Leopold et al. method.[29]

Table 1. Concentrations of reagents employed for the preparation of samples A-F and final pH of the colloidal suspensions.

[Reagent]/ mM	**A**	**B**	**C**	**D**	**E**	**F**
[$AgNO_3$]	0.07	0.37	0.73	0	0	0.73
[$HAuCl_4 \cdot 3H_2O$]	0.27	0.27	0.27	0.40	0.20	11.68
[HA]	3.00	3.00	3.00	3.00	0	3.00
[CIT]	0.26	0.26	0.26	0.26	0.77	0.03
pH	5.0	5.0	4.7	4.4	5.5	4.4

For the sake of brevity, we describe here the method leading to the Au/Ag HNS of sample A and D. 500 μL of HA ($6x10^{-2}$ M) were mixed with 500 μL of NaOH (0.05M) under vigorous stirring. Then, 9 mL of $AgNO_3$ ($1.1x10^{-4}$ M) were added at once to the first solution. This mixture was stirred during 5 min and then, 5 mL of $HAuCl_4 \cdot 3H_2O$ ($8x10^{-4}$ M) were added. Immediately after, 100 μL of CIT (1 %, w/v) were added to the final solution, heating the mixture for 5 min at 100˚C. Sample D was

prepared according to the following method: 500 µL of HA 6 x 10^{-2} M were mixed with 500 µL of NaOH (0.05 M). Afterwards, 9 mL of $HAuCl_4$ 0.44 mM were added drop wise to the first solution under agitation. After 5 min, 100 µL of trisodium citrate 4.13 x 10^{-2} M (1 %, w/v) were added to the mixture.

Preparation of Samples for SERS Spectra: A stock solution of ThT and lucigenin in water at 0.1 and 0.01 M, respectively, were prepared. Further dilutions were prepared in Milli-Q water. An aliquot of the aqueous ThT solution (typically 1 to 5 µL) at adequate concentration was then added to 1 mL of the colloidal Au/Ag HNS without any activation by aggregating agents, to get the desired final ThT concentration. SERS spectra were recorded in a glass vial focusing the laser beam inside the solution.

Instruments: Extinction spectra of the colloids were recorded on a Shimadzu 3600 spectrometer equipped with a photomultiplier tube for light detection in the UV-visible range and an InGaAs detector for NIR. Samples were placed in quartz cells of 1 cm optical path, after dilution of 30% in Milli-Q water (v/v).

SERS and Raman spectra were collected on a Renishaw Raman InVia spectrometer equipped with an electrically cooled CCD camera. Samples were excited by using the 532 nm laser line, provided by a frequency-doubled Nd:YAG laser, and a diode laser at 785 nm. Both lasers provided a final power at the sample of 2.5 mW. The spectral resolution was set in all cases to 2cm^{-1}. The final SERS spectra consisted of two scans that were registered with a total acquisition of 10s each one.

The NPs fabricated in this work were examined by using a CytoViva enhanced dark field microscope (EDFM), integrated by an illumination system (CytoViva, Auburn, AL) attached to an Olympus microscope. The system consisted of a CytoViva 150 dark field (DF) condenser in place of the microscope's original condenser, attached via a fiber optic light guide to a Solarc 24 W metal halide light source (Welch Allyn,

Skaneateles Falls, NY). A 100X immersion oil objective provided with an iris (Olympus UPlanAPO) was employed. Spectral data within each pixel of the scanned field of view were captured with a CytoViva spectrophotometer and an integrated charged-coupled device camera. The spectral data were analysed by using the CytoViva Hyperspectral analysis software program (ENVI 4.4 and ITT Visual Information Solutions) leading to the hyperspectral EDFM images. The ulterior image processing involved some steps necessary for building the spectral libraries (spectral endmembers). The spectral endmembers were obtained by the selection of a region of interest on the scanned sample. The selection allows choosing pixels that best represent the morphological state of nanoparticles. When the characteristic spectral endmembers were identified, they were saved into a spectral library for the subsequent spectral mapping of the EDFM hyperspectral images of other samples. Finally, Spectral Angle Mapper (SAM) was employed to measure the similarity between the image pixels and the endmember pixels. SAM implements by calculating the angle between the image and endmember spectra, treating them as vectors in n-D space where, n represents the number of bands. The best match was achieved when the angle between endmember and sample spectra was the least. The libraries were mapped onto images of interest by false-colouring a pixel if they were within 0.1 radians of one of the spectra in the library.

Transmission electron microscopy (TEM) images were taken using a JEOL JEM-1011 with an acceleration voltage of 100 kV equipped with an electrically cooler CCD camera.

Scanning electron microscopy (SEM) images were obtained using a Hitachi SU-6600 with an acceleration voltage of 30 kV, coupled to an energy dispersive X-ray (EDX) detector.

RESULTS AND DISCUSSION

TEM and SEM images of samples A-C are shown in Figure 2. These images clearly demonstrate that the two-step reduction process involving both HA and CIT lead to Ag nanostars, from which Au/Ag HNS are formed by a galvanic replacement and Ag redeposition method as described in the experimental part section. The simultaneous presence of Ag and Au in these NPs was confirmed by the EDX spectrum (as example, sample C in Fig. 2F).

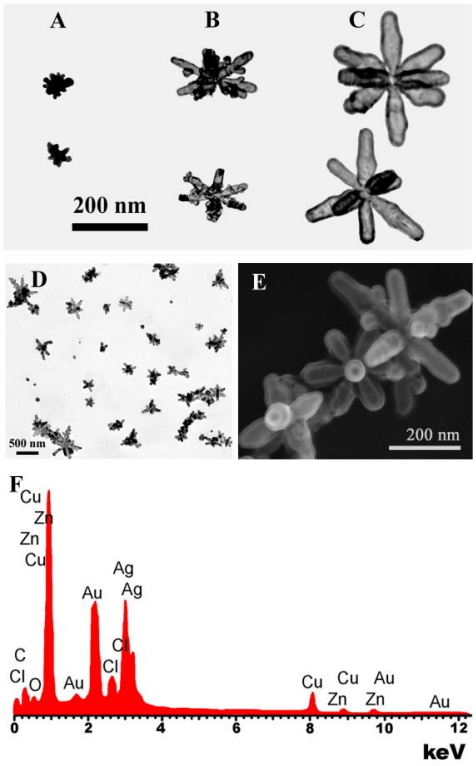

Figure 2 Micrographs of Au/Ag HNS obtained by TEM from (A) sample A, (B) sample B, and (C) sample C. For the specific case of sample C, the general view of TEM (D), the SEM (E) images and the EDX spectrum (F) are shown.

The fabrication of Au/Ag HNS strongly depends on the experimental conditions, in such a way that the final morphology can be tuned by varying the relative amounts of Ag^{+}, HA and citrate.[19] This is the reason why significant morphological differences

between HNS contained in samples A, B and C are observed. In general, the NS size becomes bigger by increasing the available amount of Ag^+ (Fig. 2A-C).

The nanoparticles of sample A have an average diameter of 40-50 nm and a big dense core from which multiple small branches emerge (Fig. 2A). The amount of silver used in the preparation of sample A is the lowest. Therefore, the nanostar arms of Au/Ag HNS undergo a lower growth regarding HNS in samples B and C, and the arm thickness is 10 nm.

Au/Ag HNS of sample B have an average diameter of 150 nm and ca 15 nm of arm width (Fig. 2B). Moreover, a clear shell of 3-5 nm is visible in the TEM images. Sample C is composed by HNS having an average diameter of 290-310 nm with 40-50 nm arm width, and a shell of ca 10 nm (Fig. 2C-D). NS of the latter sample are the biggest among all the obtained NS and are characterized by the formation of several arms (ranging from 6 to 12), which radiate from the core. The number of the arms varies from NP to NP, being eight the average number. This suggests that these NPs are grown from initial octaedrycal-shaped NPs in the formation of Ag NS templates. Sometimes these arms are branched, as occurs for example in sample B (Fig. 2B). More details of the morphology of these NPs are visible in the SEM images (see as example, sample C in Figure 2E).

As control experiments we also prepared samples D and E obtained by using only the gold(III) salt (Table 1). Au NPs in sample D, obtained from Au alone and a two-step reduction, are highly faceted with an average size ranging from 20 to 30 nm (Fig. 3D), whereas NPs in sample E, obtained in the absence of CIT, are more spherical (Fig. 3E). These control samples clearly demonstrated that the presence of Ag is the only way to reach the star-size morphology, and that the galvanic replacement from starting Ag NS is a crucial condition to get hollow nanostars.

As predictable, the morphological differences in NPs induced a strong change in the colloidal suspension color (Inset of Figure 3). For example, the increase of the $AgNO_3$ concentration (Table 1), induces a color change from clear blue, in the colloidal suspension of sample A, to dark blue in sample B. The extinction spectra of the colloidal NP suspensions showed that the samples containing nanostars (samples A, B, and C) give rise to maxima at 725, 600, and 680 nm, respectively (Figure 3). These peaks are shifted to higher wavelengths in relation to the case of Au NPs of sample D (strong peak at 540 nm) and the spherical Au NPs of sample E (maximum at 520 nm). The differences observed in the extinction spectra of the latter samples are due to the variable morphology of the template Ag NS which leads to a different exposed Ag surface for the galvanic replacement.

It is noteworthy noting that the extinction maximum of sample A appears at higher wavelengths in comparison to the other samples, even if its NS are smaller than those in samples B and C. In addition, it is difficult to assess whether the NS contained in this sample are hollow or compact, since no void space can be seen in the TEM images. This result is attributed to the fact that in the latter sample the amount of atoms employed to fabricate the initial Ag NPs is ten times lower than that used in the sample C, thus leading to a lower number of NPs and a smaller size in comparison with those contained in sample C. Since the number of Au atoms is the same in the two methods, the gold shell formed around the NS particles of sample A is thicker than that existing in the sample C, and even the nanostar can have a compact structure with no void space in the inner part. Furthermore, the amount of Ag redeposited is lower. This effect is the responsible for the shift towards higher wavelengths of the overall extinction spectrum.

In general, the broad extinction background observed in NS suspensions can be attributed to the different absorption and scattering emissions produced by the large

variety of NPs forming part of the suspension with low effect from the aggregation of nanoparticles. In fact, these NS exhibit different morphologies with different number of arms and different tip sharpness. The mixture of all this factors leads to very different localized surface plasmon resonances, since a wide range of wavelength in the visible and near-IR range can be covered with various NS shapes.[14,30,31]

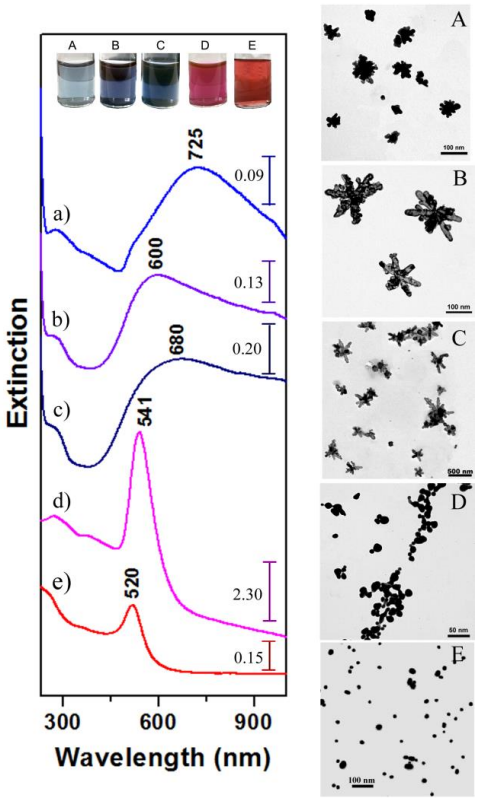

Figure 3 Extinction spectra (left) and TEM images (right) corresponding to the samples: A (a), B (b), C (c), D (d) and E (e). *Inset:* Pictures of colloids obtained from the A, B, C, D and E samples.

In order to get more insight about the plasmon resonance of individual NS, scattering spectra from single nanoparticles were recorded by a hyperspectral analysis of the EDFM images. The SAM classification images showed the distribution of all the spectral profiles in the images (endmember number up to 7), as well as the quantification of their relative abundance. For the sake of brevity, EDFM images of samples C and D are shown in Figure 4, together with the most representative scattering spectra from the individual NPs. In addition, the spectral maps are shown, displaying

the relative distribution of the main plasmon resonances by false-colouring pixels if the mapped libraries were within 0.1 radians of one of the spectra in the library.

Light scattering of HNS in sample C (Fig. 4a) gave rise to only four main spectral signatures, at 547 (green), 620 (yellow, with a shoulder at 530 nm), 641 (orange) and 690 nm (purple), due to a more homogeneous distribution of NP sizes. The corresponding class distribution indicated that the peak at 620 nm represents the main contribution to the total scattering of the sample since it contributes to 62 % of the measured scattering plasmon spectra of individual nanoparticles and can be attributed to the NS morphology of this sample normally observed in TEM images (Fig. 2D).

As regards sample D, it displays a rather heterogeneous distribution of NPs evidenced by the large amount of different scattering spectra peaking in the 500-700 nm region (Fig. 4b). This behavior can be attributed to the broad distribution of morphology (size and shape) of the faceted NPs integrating this sample (Fig. 3D). A high number of aggregates (dimers, trimers and bigger aggregates) can be also formed during the drying

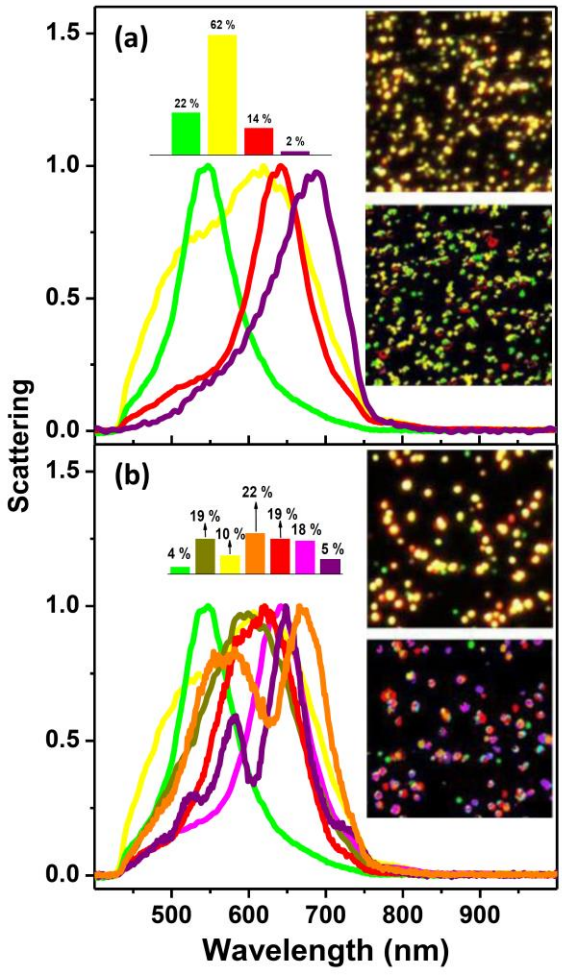

process, as visible in the TEM images.

Figure 4 The scattering spectra observed in samples: C (a) and D (b) obtained from the hyperspectral analysis. Inset: EDFM images (up) and their spectral map (down) with colored area indicating the matching with the spectral endmembers. Relative percentage abundance of the spectral profiles, revealed by the SAM analysis of the hyperspectral images, is also displayed. All the EDFM and SAM images are 15 μm x 15 μm.

The metallic composition of the surface on NS resulting from the galvanic replacement was examined by using lucigenin as molecular probe. This molecule is known to have a different SERS spectrum on Ag and Au metals.[32] Thus, the SERS spectra of lucigenin were obtained by using colloidal HNS suspensions prepared with different Au/Ag ratio (methods C and F in Table 1), and compared with those obtained on Ag and Au NPs (Figure 5). The morphology of nanoparticles included in the sample F was not previously characterized by TEM, because the main interest of this sample was the preparation of nanoparticles with a high Au/Ag ratio. The presence of the strong Metal-Cl^- stretching band in the 244-254 cm^{-1} region (provided by the initial Au salt) and the high similarity of the lucigenin SERS spectrum with that observed on Ag NPs indicates the presence of Ag atoms in the hollow nanoparticle shell, even if the Au/Ag ratio used for obtaining HNS is raised up to 16 (sample F in Figure 5). This is attributed to the stronger affinity of lucigenin for Ag. However, the exact proportion of Ag in relation to Au on the surface of these NPs is difficult to assess due to these differences in affinity.

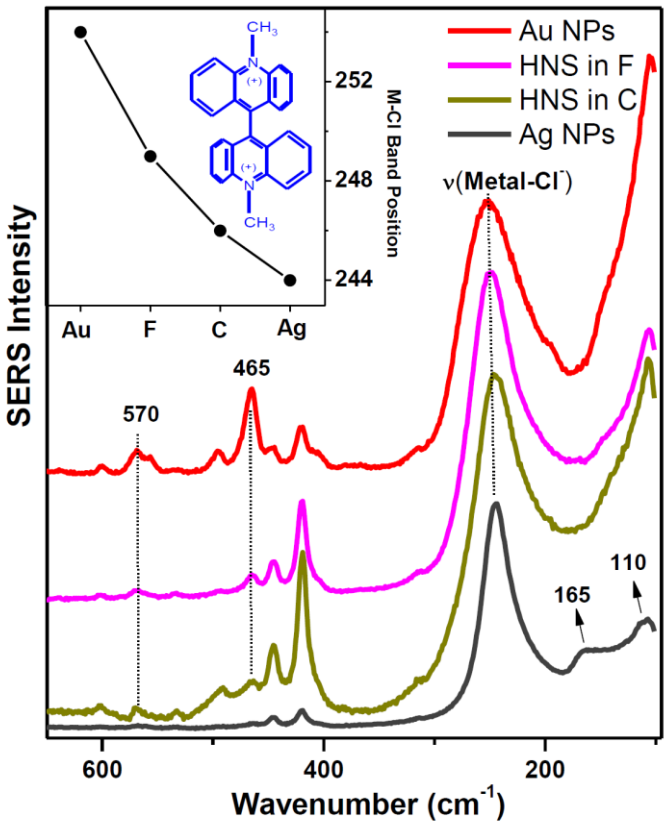

Figure 5 Low wavenumber region of SERS spectra of lucigenin on the following metal substrates: Ag NPs, Au NPs, and HNS of samples C and F, respectively. Inset: chemical structure of lucigenin and dependence of the ν(Metal-Cl$^-$) band position in the SERS spectra obtained by using different NPs. This trend is strongly dependent from the Au content. These spectra were obtained by using the laser at 785 nm.

Moreover, a possible indication on the Au/Ag ratio can be deduced from the position of the ν(Metal-Cl$^-$) band plotted in the inset of Figure 5 for the analyzed samples: the less the Au content, the stronger is the band shift towards lower wavenumbers.

In addition, the disappearance of the features at 165 and 110 cm^{-1}, attributable to the existence of Ag clusters on the surface of the Ag nanoparticles[33], and the intensification of lucigenin bands characteristic of the Au surface (at 465 and 570 cm^{-1}), clearly indicate that the HNS are integrated by both Au and Ag atoms which form an actual alloy shell with a nanostar shape, in agreement with the EDX analysis (Fig. 2).

The effectiveness of the NS fabricated in this work in the SERS detection was monitored by using ThT as probe molecule. Figure 6a shows the Raman spectrum of an

aqueous solution of ThT (10 mM) and the SERS spectra of ThT registered on sample B (Fig. 6b) and the spherical Au NPs of the sample E without adding aggregating agents (Fig. 6c). The most evident result from these experiments is the complete absence of signal from ThT adsorbed onto Au NPs, in contrast to the strong SERS spectrum obtained on HNS of sample B, showing strong bands at 530, 696, 743, 795 and 1033 cm^{-1}. This demonstrates the existence of a large amount of hot spots in the vortexes existing in NS, leading to strong plasmonic intensification of the signal without the need of aggregation. The minimum ThT concentration detected on HNS obtained by method B was 10^{-8} M.

The SERS enhancement also depends on the excitation wavelength and the substrate used. Figure 6d shows the variation of the intensity of the most intense bands from the SERS of ThT recorded by exciting at 532 (1545 cm^{-1}) and 785 nm (530 cm^{-1}). All the SERS spectra are shown in the Supporting Information. It is to note that the band at 1545 cm^{-1} shows the maximum intensity in the Sample C , while at 785 nm the colloidal suspension of sample A provides the most intense spectrum. This can be explained on the basis of the extinction spectra of each sample (Fig. 3), since the line at 532 nm is close to the plasmon resonance of sample C, while at 785 nm is closer to the sample A resonance. The enhancement factors calculated for ThT using the 785 and 532 nm excitation lines and the different substrates are summarized in Table 2. As can be seen, NS of samples A-C display a significant SERS activity for both excitations, while Au NPs of samples D-E are active only in the red spectral region, thus following the plasmon resonance of Au. The large enhancement observed for sample D is due to the aggregation of the colloid in the presence of ThT.

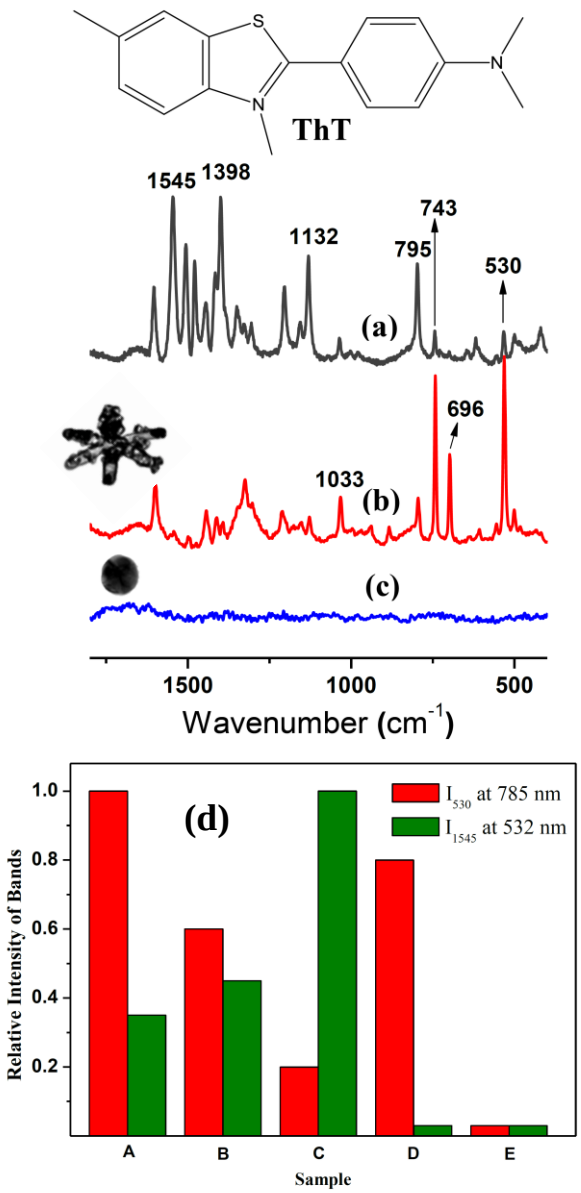

Figure 6 Raman spectrum of ThT 10 mM (a) and the SERS spectra of ThT 1 μM obtained on samples B (b) and E (c), at the excitation wavelength of 785 nm. (d) SERS enhancement dependence on the excitation wavelength and the colloidal suspension used: 532 nm and 785 nm. A, B, C, D and E correspond to the samples indicates in the Table 1. This enhancement dependence was normalized to the maximum value in each case.

Table 2: Enhancement Factor calculated for ThT at a final concentration of 1 μM on different substrates and excitation wavelengths. These factors were calculated by the following expression: $EF=I_{SERS}xC_{sol}/I_{sol}xC_{SERS}$, where I_{SERS} is the intensity of the most intense band for each excitation wavelength; C_{sol} is the concentration of the aqueous solution; I_{sol} is the intensity of the same band in the solution and C_{SERS} is the concentration of ThT in the SERS experiement.

Exitation Line (nm)	**Sample A**	**Sample B**	**Sample C**	**Sample D**	**Sample E**
785	2.28×10^5	1.21×10^4	3.57×10^3	1.35×10^5	2.92
532	5.92×10^3	8.17×10^3	1.29×10^4	No signal	No signal

The investigation of spectral changes in SERS spectra is also noteworthy in the elucidation of the adsorption process occurring on these NPs. By comparing the Raman spectra of ThT in aqueous solution (Fig. 6a) and the SERS spectrum on the metal nanostars (Fig. 6b), many changes are observed, such as modifications in the relative band intensity, appearance of new bands, and band widening or shifting. In particular, the bands at 531, 696, 743, 795 and 1033 cm^{-1} are enhanced in the SERS spectra at all concentrations. Since many of these bands are due to the δ(CSC) motion[34], an interaction of ThT through the sulfur atom of the benzothiazole moiety with the metal surface can be deduced. On the other hand, the bands at 1545, 1506 and 1398 cm^{-1}, seen in the Raman of the aqueous solution (Fig. 6a), disappear in the SERS spectrum. The intensity decrease of the later bands is connected to the electronic resonance lowering between aromatic rings, which in turn is related to the rotation of the two aromatic parts of ThT once interacting with the metal NPs.

On the other hand, other relative intensity changes can be rather attributed to the influence of different excitation wavelengths on both the plasmon and molecular resonance. For instance, it is observed a higher intensification of bands in the lower wavenumber region for the sample A at 785 nm (Fig. 7b). This is attributed to the

decreasing plasmonic extinction in this spectral range (Fig. 7c). On the other hand, the SERS spectrum of ThT is weaker at 532 nm (Fig. 7a), because of the low extinction at this wavelength (Fig. 7c). Conversely, sample C gives rise to a SERS spectrum more intense at 532 nm (Fig. 7f) than at 785 nm (g) due to the increased plasmonic extinction in this spectral range (Fig. 7d).

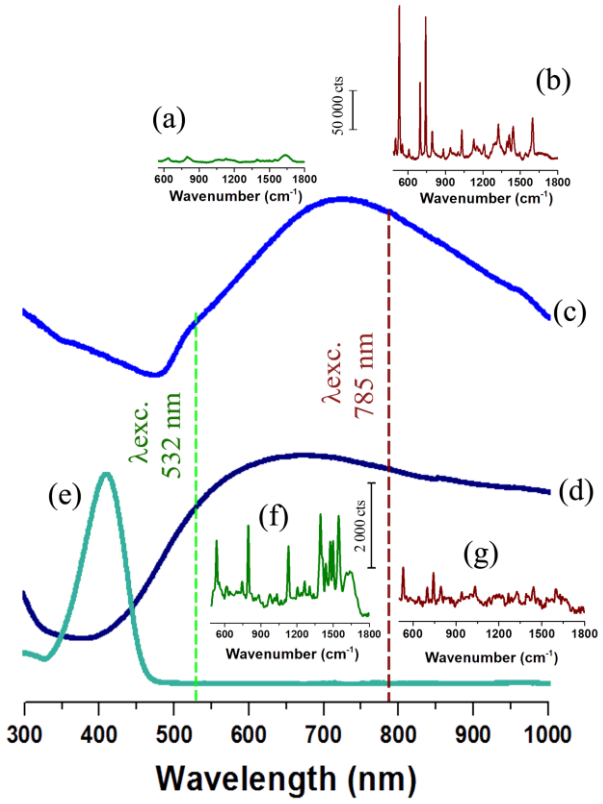

Figure 7. SERS spectra of ThT obtained by using different substrates and excitation lines: sample A and excitation at 532 nm (a) and 785 nm (b) and sample C and excitation at 532 nm (f) and 785 nm (g). The extinction spectra of samples A (c) and C (d) and the absorption spectrum of ThT (0.1 M) in water (e) were also shown for comparison.

CONCLUSIONS

Hollow Au/Ag nanostars with different morphologies were successfully prepared by a method combining the classical chemical reduction and the galvanic replacement method. Four preparation methods differing in the relative Au/Ag concentration ratio, as well as the concentration of the two employed chemical reductors

(hydroxylamine and citrate) were defined and tested for SERS applications. In general, the size of the resulting nanostructures, as well as the arm thickness, increases by increasing the available amount of Ag^+ ions. The average number of arms in HNS are eight, indicating that these NPs are initially grown from octaedrycal-shaped NPs, and the average diameters range from 30 nm to 350 nm with Au/Ag shell thickness of 3-10 nm.

The plasmonic resonance of the prepared NS is extremely sensitive to changes in shape and size which can be tuned on the basis of the different method employed in their fabrication. The shells observed in the HNS are integrated by an alloy of both Au and Ag as deduced from the EDX spectra and also from the SERS spectra of chloride and lucigenin employed to examine the surface.

The NS obtained in this work exhibit a large SERS activity thanks to large amount of hot spots on the surface, so it was not necessary the addition of any aggregation agent. Consequently, these NS particles have a large free surface which makes easier the analyte absorption. The latter feature is one of the major advantages of the Au/Ag NS reported here regarding the conventional Au NS. In addition these NS have a more universal SERS activity, irrespective of the excitation wavelength.

In general, all bimetallic star-shaped NPs have a SERS activity in all the visible and near IR regions, although some differences exist. NS of sample A exhibits the maximum intensification of SERS spectrum in the red spectral region, whereas those obtained by method C are more active by using the 532 nm excitation line. This is due to the significant modification in the extinction spectra depending on the different morphologies.

The results presented in this work demonstrate that bimetallic hollow nanostars fabricated in this work have promising optical and chemical properties to be used for

different applications: spectroscopy, sensing, drug delivery or theranostic, and, indeed, more research is now needed to investigate these applications.

ACKNOWLEDGMENTS

This work has been supported by the Spanish *Ministerio de Economía y Competitividad* (MINECO, grant FIS2014-52212-R). A. G.-L. acknowledges CSIC and FSE 2007-2013 for a JAE-CSIC predoctoral grant. Srdja Drakulic is acknowledged for TEM measurements. The authors are grateful to Dr. Carla Marzetti (Antigenia srl Unipersonale), Italian contact person of Cytoviva company, for providing the hyperspectral CytoViva® microscopy.

REFERENCES

(1) Schütz, M.; Steinigeweg, D.; Salehi, M.; Kömpe, K.; Schlücker, S. *Chem. Comm.* **2011**, *47*, 4216.
(2) Senthil Kumar, P.; Pastoriza-Santos, I.; Rodríguez-González, B.; Javier García De Abajo, F.; Liz-Marzán, L. M. *Nanotechnology* **2008**, *19*.
(3) Khoury, C. G.; Vo-Dinh, T. *J. Phys. Chem. C* **2008**, *112*, 18849.
(4) Chen, H.; Zhang, X.; Dai, S.; Ma, Y.; Cui, S.; Achilefu, S.; Gu, Y. *Theranostics* **2013**, *3*, 633.
(5) Fales, A. M.; Yuan, H.; Vo-Dinh, T. *Mol. Pharm.* **2013**, *10*, 2291.
(6) Liu, Y.; Yuan, H.; Fales, A. M.; Tuan, V.-D. *J. Raman Spectrosc.* **2013**, *44*, 980.
(7) Ma, W.; Sun, M.; Xu, L.; Wang, L.; Kuang, H.; Xu, C. *Chem. Comm.* **2013**, *49*, 4989.
(8) Osinkina, L.; Lohmueller, T.; Jaeckel, F.; Feldmann, J. *J. Phys. Chem. C* **2013**, *117*, 22198.
(9) Yuan, H.; Liu, Y.; Fales, A. M.; Li, Y. L.; Liu, J.; Vo-Dinh, T. *Anal. Chem.* **2013**, *85*, 208.
(10) Lee, J.; Hua, B.; Park, S.; Ha, M.; Lee, Y.; Fan, Z.; Ko, H. *Nanoscale* **2014**, *6*, 616.
(11) Vo-Dinh, T.; Fales, A. M.; Griffin, G. D.; Khoury, C. G.; Liu, Y.; Ngo, H.; Norton, S. J.; Register, J. K.; Wang, H.-N.; Yuan, H. *Nanoscale* **2013**, *5*, 10127.
(12) Hao, F.; Nehl, C. L.; Hafner, J. H.; Nordlander, P. *Nano Lett.* **2007**, *7*, 729.
(13) Song, H. M.; Deng, L.; Khashab, N. M. *Nanoscale* **2013**, *5*, 4321.
(14) Rodriguez-Oliveros, R.; Sanchez-Gil, J. A. *Optics Express* **2012**, *20*, 621.
(15) Guerrero-Martínez, A.; Barbosa, S.; Pastoriza-Santos, I.; Liz-Marzán, L. M. *Curr. Opin. Colloid In.* **2011**, *16*, 118.
(16) Li, M.; Cushing, S. K.; Zhang, J.; Lankford, J.; Aguilar, Z. P.; Ma, D.; Wu, N. *Nanotechnology* **2012**, *23*.
(17) Nalbant Esenturk, E.; Hight Walker, A. R. *J. Raman Spectrosc.* **2009**, *40*, 86.

(18) Rodríguez-Lorenzo, L.; Krpetic, Z.; Barbosa, S.; Alvarez-Puebla, R. A.; Liz-Marzán, L. M.; Prior, I. A.; Brust, M. *Integr. Biol.* **2011**, *3*, 922.

(19) Garcia-Leis A., G.-R. J. V., and Sanchez-Cortes S. *J. Phys. Chem. C* **2013**, *117*, 5.

(20) Mahmoud, M. A.; O'Neil, D.; El-Sayed, M. A. *Chem. Mat.* **2014**, *26*, 44.

(21) Mahmoud, M. A.; Narayanan, R.; El-Sayed, M. A. *Acc. Chem. Res.* **2013**, *46*, 1795.

(22) Yin, J.; Zang, Y.; Xu, B.; Li, S.; Kang, J.; Fang, Y.; Wu, Z.; Li, J. *Nanoscale* **2014**, *6*, 3934.

(23) Xia, X.; Wang, Y.; Ruditskiy, A.; Xia, Y. *Adv. Mater.* **2013**, *25*, 6313.

(24) Tian, L.; Gandra, N.; Singamaneni, S. *Acs Nano* **2013**, *7*, 4252.

(25) Rivas, L.; Sanchez-Cortes, S.; Garcia-Ramos, J. V.; Morcillo, G. *Langmuir* **2000**, *16*, 9722.

(26) Liz-Marzan, L. M. *Langmuir* **2006**, *22*, 32.

(27) Sun, Y. G.; Mayers, B. T.; Xia, Y. N. *Nano Lett.* **2002**, *2*, 481.

(28) Frens, G. *Nat. Phys. Sci.* **1973**, *241*, 20.

(29) Cañamares, M. V.; Garcia-Ramos, J. V.; Gomez-Varga, J. D.; Domingo, C.; Sanchez-Cortes, S. *Langmuir* **2005**, *21*, 8546.

(30) Giannini, V.; Rodriguez-Oliveros, R.; Sanchez-Gil, J. A. *Plasmonics* **2010**, *5*, 99.

(31) Ma, W. Y.; Yang, H.; Hilton, J. P.; Lin, Q.; Liu, J. Y.; Huang, L. X.; Yao, J. *Optics Express* **2010**, *18*, 843.

(32) Guerrini, L.; Garcia-Ramos, J. V.; Domingo, C.; Sanchez-Cortes, S. *J. Raman Spectrosc.* **2010**, *41*, 508.

(33) Sanchez-Cortes, S.; Garcia-Ramos, J. V.; Morcillo, G.; Tinti, A. *J. Coll. Interface Sci.* **1995**, *175*, 358.

(34) Lopez-Tobar, E.; Antalik, M.; Jancura, D.; Canamares, M. V.; Garcia-Leis, A.; Fedunova, D.; Fabriciova, G.; Sanchez-Cortes, S. *J. Phys. Chem. C* **2013**, *117*, 3996.

Graphical Abstract